Chinese Chemical Letters 33 (2022) 2681–2686

Contents lists available at ScienceDirect

Chinese Chemical Letters

journal homepage: www.elsevier.com/locate/cclet

High-energy aqueous supercapacitors enabled by N/O codoped carbon nanosheets and "water-in-salt" electrolyte

Jingjing Yan[b], Ling Miao[a,*], Hui Duan[a], Dazhang Zhu[a], Yaokang Lv[d], Liangchun Li[a], Lihua Gan[a], Mingxian Liu[a,c,*]

[a] Shanghai Key Lab of Chemical Assessment and Sustainability, School of Chemical Science and Engineering, Tongji University, Shanghai 200092, China
[b] School of Chemical Engineering, Anhui University of Science and Technology, Huainan 232001, China
[c] College of Chemistry and Molecular Engineering, Zhengzhou University, Zhengzhou 450001, China
[d] College of Chemical Engineering, Zhejiang University of Technology, Hangzhou 310014, China

ARTICLE INFO

Article history:
Received 10 June 2021
Revised 18 August 2021
Accepted 30 August 2021
Available online 4 September 2021

Keywords:
Porous carbon nanosheets
N/O codoping
Water-in-salt electrolyte
High-energy supercapacitor

ABSTRACT

A facile fabrication strategy is reported to obtain N/O codoped porous carbon nanosheets for purpose of ameliorating the charge transfer and accumulation in the concentrated LiTFSI (lithium bis(trifluoromethane sulfonyl)imide) electrolyte. By tunning the feed ratio of comonomers, the porous nanosheet structure is endowed with a significant ion-adsorption surface area (1630 m^2/g) and interconnected hierarchical porosity; meanwhile, high-level N/O dopants (N: 3.58 at%, O: 12.91 at%) increase the effective contact area for electrolyte ions, and further facilitate rapid ion/electron transfer. Benefiting from the advantageous features, carbon nanosheets electrode reveal an enhanced specific capacitance (375 F/g) in three-electrode configuration and the H_2SO_4-based device yields a high gravimetric energy density of 11.4 Wh/kg. Particularly, the ion-diffusion highways in porous carbon nanosheets contribute to the 2.25 V LiTFSI-based symmetric device with a high energy delivery up to 33.1 Wh/kg. This work offers an inspiring strategy for facile fabrication of carbon nanosheets, and demonstrates their promising application in "water-in-salt" electrolyte-based supercapacitor systems.

Carbon-based aqueous supercapacitors (CASs) with fast charge/discharge process, superior cyclic stability and high power density, have received tremendous attention in both theoretical and industrial researches in recent years [1-4]. Whereas, the lower energy densities of CASs relative to non-aqueous ones hinder their large scale applications, and thus achieving high energy density is of vital importance for these promising devices. According to the equation of energy density: $E = 1/2CV^2$ [5,6], the specific capacitance (C) and voltage window (V) are two pivotal parameters for energy density of CASs. The specific capacitance is strongly related to the surface area, porous structure and heteroatom doping of carbon-based electrodes [7,8]. And the voltage window mainly depends on the composition and concentration of the electrolytes [6,9-11]. Therefore, exploiting the high-capacitance carbon electrode with large over-voltage window for hydrogen/oxygen evolution is a desirable avenue to achieve the high energy density for alleviating the future energy demands.

Carbon nanosheets are considered as superior electrode materials in terms of their well-developed porosity, open-ended porous architecture and continuous conductive pathways [12-15]. For example, Wei and coworkers designed 3D hierarchical carbons with cross-linked porous sheets [16], wherein multi-level porous channels in carbon nanosheets conduce to fast ion transport and efficient electrolyte permeation, thereby generating a high energy delivery of 31.9 Wh/kg in 2.2 V $ZnSO_4$ electrolyte. However, carbon nanosheets generally exhibit a tendency to self-restack and/or aggregate during the thermal process, resulting in a significant loss of active ion-adsorption area and a decreasing overall capacitance [17]. Therefore, establishing porous carbon nanosheets with large ion-adsorption area, high-level heteroatom decoration and hierarchical porous architecture is a remarkable challenge in pursuit of high-performance supercapacitors. Furthermore, the well-designed porous carbon nanosheets should combine the following characteristics of: (1) the interconnected carbon nanosheets can provide the enhanced specific surface area and abundant electroactive sites for ion-adsorption [18,19]; (2) large specific surface area can facilitate charge accommodation at electrode/electrolyte interphase [20-22]; (3) hierarchical porous structure can accelerate the ef-

* Corresponding authors.
E-mail addresses: 1310593@tongji.edu.cn (L. Miao), liumx@tongji.edu.cn (M. Liu).

https://doi.org/10.1016/j.cclet.2021.08.123
1001-8417/

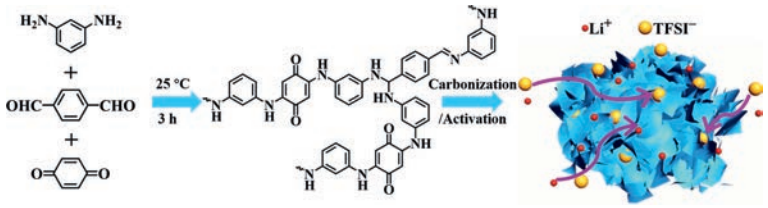

Fig. 1. Schematic illustration of the synthesis of MPK_x.

fective electrolyte permeation and promote charge transfer kinetics [15,23,24]; (4) heteroatom-containing groups can improve the surface accessibility and electron conduction, coupled with inducing extra *pseudo*-capacitance [25,26]. Recently, considerable efforts have been devoted to constructing heteroatom-doped, hierarchically porous carbon nanosheets either by solvothermal strategies or lithographic patterning [27-29]. Since multi-stepped procedures or additional etching treatments are still required in the synthesis process, great expectations are still placed on developing a simple route to construct carbon nanosheets as high-performance supercapacitor electrodes.

Equally important, the energy density is in positive proportion to the square of the potential window, indicating that the increased effective potential window is significantly conducive to the enhanced energy generation of supercapacitor. The organic electrolytes and ionic liquids are known to furnish an electrochemical stability window greater than 3 V, which contributes to a high-energy configuration. However, complicated purification and manufacturing, low conductivity, high flammability and toxicity of organic electrolytes and ionic liquids raise extra concerns [30,31]. By comparison, aqueous electrolytes outperform better in above mentioned problems except for the inherent narrow voltage window (~1.23 V) [32]. Furthermore, the pseudocapacitive materials using aqueous electrolytes can occur Faraday redox reactions, consequently generating the extra pseudocapacitance. Quite recently, researchers have reported that the "water-in-salt" electrolyte (lithium bis(trifluoromethane sulfonyl)imide, LiTFSI) could broaden the voltage window for aqueous supercapacitors [33], as a majority of water molecules incorporate with Li^+ and participate in the solvation sheaths, consequently hindering the free water decomposition for an enlarged electrochemical stability window [30,34]. However, the low conductivity and high viscosity deteriorating the ion diffusibility will be expected to surmount for carbon nanosheet-based supercapacitors employing "water-in-salt" electrolytes.

Herein, we reported a facile cost-economical and time-saving approach for constructing N/O dual-doped carbon nanosheets (MPK_x) with the contiguous open porous channels. The large ion-adsorption surface area (1630 m^2/g) and the interconnected conductive framework in porous carbon nanosheets, together with high-doping N/O species (N: 3.58 at%, O: 12.91 at%), result in an enhanced gravimetric capacitance of 375 F/g in a three-electrode configuration using H_2SO_4 electrolyte. The typical carbon nanosheets-based symmetric devices generate a high specific energy of 11.4 Wh/kg in H_2SO_4. Moreover, the ion-infiltration highways in porous carbon nanosheets contribute to the 2.25 V LiTFSI-based symmetric device with a high energy delivery up to 33.1 Wh/kg, together with a capacitance retention of 91% after 10000 charge/discharge cycles.

The synthesis process of MPK_x is schematically illustrated in Fig. 1. Firstly, terephthalaldehyde (TPA) is mixed with excessive *m*-phenylenediamin (PLD) by using *p*-toluenesulfonic acid as catalyst to prepare TPA/PLD intermediate blend ($PMPK_0$, Fig. S1a in Supporting information) with reversible imine bonds prior to the participation of *p*-benzoquinone (BZQ). The conjugated-bond TPA/PLD/BZQ intercondensation polymer ($PMPK_2$) with compact sheet-like architecture is reassembled by the mixture of highly active BZQ and the intermediate oligomer TPA/PLD with reversible imine bond (Fig. S1b in Supporting information). The structures of $PMPK_x$ with similar spectra are characterized by FT−IR spectra (Fig. S2 in Supporting information). The typical absorption peaks at 1605 and 1690 cm^{-1} are the corresponding stretching vibration of C=N (the typical skeleton characteristic in TPA/PLD) and C=O (deriving from TPA and/or BZQ) [35,36]. The peak at 1590 cm^{-1} originates from the stretching vibration of C=C [37], and the bending vibration of N-H at 3340 cm^{-1} reflects the presence of a secondary amine [38].

The morphologies of the sheet-dominated MPK_x are characterized using SEM and TEM. A SEM image of $PMPK_0$ (Fig. S1a) exhibits a spherical structure with the average diameter of ~660 nm. A layered porous architecture with microsized cavities connected through coalescent carbon sheets in MPK_0 (Figs. 2a and e) are generated, resulting from the TPA/PLD intermediate blend pyrogenic decomposition together with the sublimation of inner molecular volatile matter. Then, by the addition of BZQ into the $PMPK_0$ condensation system, the established sheet-like $PMPK_1$ (Fig. S1b) is derived from the reaction between highly active BZQ and TPA/PLD oligomer and finally transformed into MPK_1 with a crumpled sheet (Figs. 2b and f) after carbonization/activation function of KOH. As BZQ dosage increasing, the loose sheets with nano-thickness for MPK_2 with well-developed open pores (Figs. 2c and g) are originated from the regular leaf-like $PMPK_2$ copolycondensate (Fig. S1c in Supporting information). High-resolution TEM (lower left corner inset in Fig. 2g) reveals that the MPK_2 nanosheets are essentially amorphous carbon with distorted graphite layers (Fig. 2g). Furthermore, a tremendous of white dots can be observed, demonstrating the existence of abundant micropores. With the amount of BZQ up to 3 mmol, the leaf-like $PMPK_3$ (Fig. S1d in Supporting information) are evolved into MPK_3 composing of dense and interconnected carbon nanosheets (Figs. 2d and h). Therefore, the participation of BZQ has a significant effect on the copolycondensation kinetics into reassemble a frizzy and loose layer architecture, and the open coalescent channels in carbon nanosheets are highly available for electrolyte ion adsorption and continuously smooth transport, as well as shorten the diffusion highways of ions. Moreover, the morphology and heteroatom doping of N and O elements within porous carbon nanosheets are preliminarily characterized by EDS element mapping apparatus. The EDS elemental mappings (Figs. 2i−k) of MPK_2 reveal the homogenous distribution of N and O elements in the carbon matrix, which reflects the sheet-like framework distribution of these elements (Fig. 2l).

XPS tests are further implemented to analyze the surface elemental content and the chemical state for each MPK_x sample. The XPS survey (Fig. 3a) confirms that nitrogen and oxygen species are successfully incorporated into the MPK_x skeleton. The high-resolution N 1s spectra of MPK_x are deconvoluted into four fitted peaks (Figs. S3a−d and Table S1 in Supporting information), which are assigned to pyridinic nitrogen (398.2 eV, N-6), pyrrolic or pyridonic nitrogen (399.5 eV, N-5), graphitic or quaternary nitrogen (400.3 eV, N-Q) and oxidized nitrogen (401.6 eV, N-X), re-

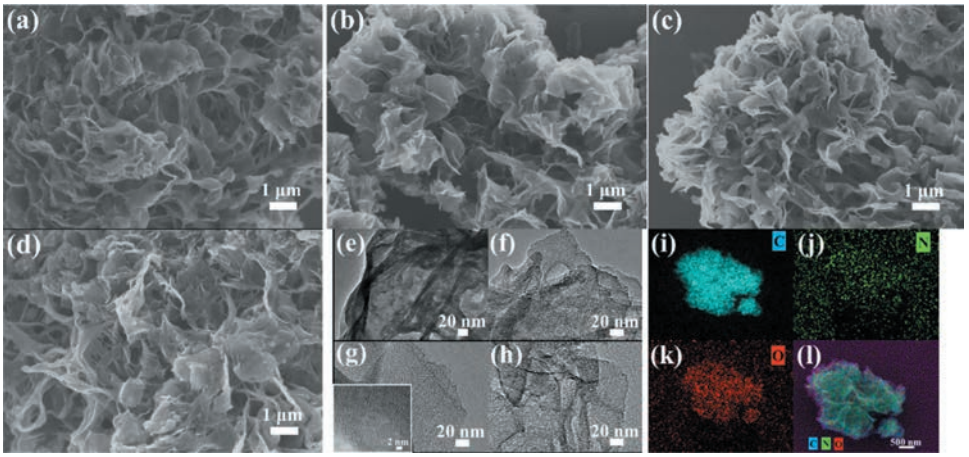

Fig. 2. SEM images of MPK_0 (a), MPK_1 (b), MPK_2 (c) and MPK_3 (d). TEM images of MPK_0 (e), MPK_1 (f), MPK_2 (g, inset is the high-resolution TEM image) and MPK_3 (h). EDS elemental mappings of MPK_2: C (i), N (j), O (k) and overlapped elemental mapping images of C, N and O in MPK_2 (l).

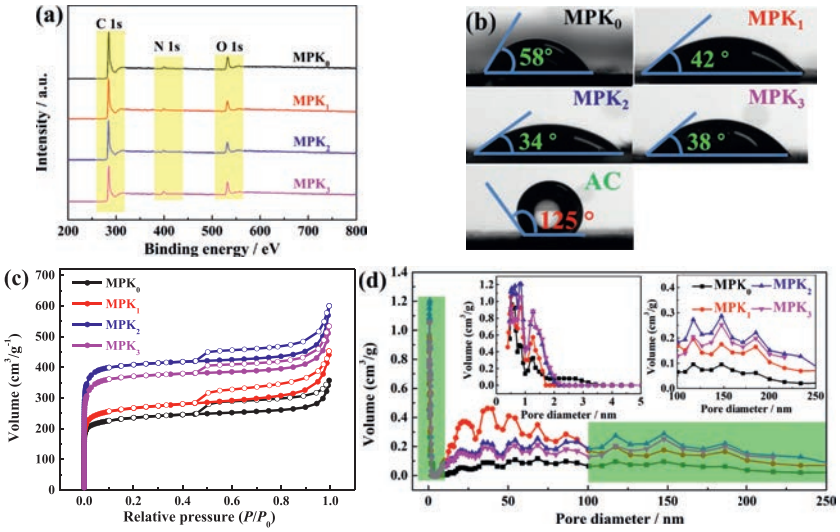

Fig. 3. XPS spectra of MPK_x (a). Wetting angles of water droplet on the surface of MPK_x and activated carbon (AC) (b). N_2 adsorption-desorption isotherms (c) and pore size distribution (d) of MPK_x.

spectively [39]. N-5 and N-6 can create the electroactive sites and defects to yield more open channels, together with introduction of the extra pseudocapacitance. N-Q can significantly ameliorate electron transfer to achieve the increased electronic conductivity and rapid charge transmission [40,41]. The high-resolution O 1s spectra (Figs. S3e–h and Table S1 in Supporting information) exhibit three fitted peaks at 530.7, 532.1 and 533.6 eV, corresponding to O-1 (C=O), O-2 (C–OH and/or C–O–C) and O-3 (COO–), separately [36]. The conjugated carbon bonded with electron-rich oxygen can regulate sufficient electron density located on the surface of carbons [42,43]. Furthermore, the dopant oxygen is beneficial to the electrolyte ions easily accessible to the polarized surface and rapid ion transport, resulting in an enhanced integral capacity [44,45]. The synergistic effect of N/O dopants is further confirmed by the contact angle using water droplets on the surface of MPK_x. Compared with hydrophobic AC (125°), MPK_x samples are hydrophilic with the contact angles ranging from 34–58° (Fig. 3b), implying the excellent wettability. In particular, the lowest contact angle (34°) of MPK_2 demonstrates the highly hydrophilic feature due to the efficient employment of ion-adsorption area furnished by its highest heteroatom contents.

N_2 adsorption-desorption isotherms for MPK_x samples (Fig. 3c) exhibit type I isotherm feature with a steep increase at $P/P_0 = 0.05$, indicating the existence of abundant micropores [15]. Meanwhile, the hysteresis loop at $P/P_0 = 0.4$–0.95 and the sharply rise at $P/P_0 = 0.95$–1.0 suggest the coexistence of micro-, meso- and macroporous structure [46], which is also confirmed by pore size distribution profiles (Fig. 3d). Detailed structural information is demonstrated in Table S2 (Supporting information). As the increasing BZQ, the specific surface areas increase from 908 m^2/g (MPK_0) to 1630 m^2/g (MPK_2) and then decreases to 1464 m^2/g (MPK_3), owing to the reassembled nanosheets and frizzy structures with ample interconnected open macropore. The abundant micropore is mostly concentrated at *ca.* 0.5, 0.8 and 1.2 nm (Fig. 3d), contributing to the supreme micropore surface area (1573 m^2/g) and micropore volume (0.61 cm^3/g). XRD patterns (Fig. S4a in Supporting information) display two typically broad peaks located at 26 and 44° corresponding to the planes of (002) and (100), revealing the amorphous carbon characteristic [16,47], which is consistent with the TEM analysis. Raman spectra of all MPK_x samples in Fig. S4b (Supporting information) exhibit two prominent peaks at 1345 (D band, disordered and defect feature) and 1590 cm^{-1} (G band, graphitic feature) [26,48]. The intensity ratios between D band and G band (I_D/I_G) for MPK_x are 0.93 except for MPK_0 (0.85). Thus, the introduction of BZQ into copolycondensate system not only furnishes a superior ion-accessible multiscale porous struc-

ture and a high surface area (1630 m^2/g), but also generates the intrinsic defects for carbon nanosheets to generate extra pseudocapacitance.

Electrochemical evaluation of all the MPK_x electrodes is examined in a three-electrode configuration with 1 mol/L H_2SO_4 aqueous electrolyte. All CV curves (Fig. S5a in Supporting information) of MPK_x electrodes at 10 mV/s present roughly rectangular shapes with two conspicuous redox peaks at around 0.2−0.6 V attributed to the redox reaction derived from nitrogenous/oxygenated functional groups in MPK_x skeleton [49], reflecting the coexistence of electric double-layer capacitance (EDLC) and pseudocapacitance. By comparison, the CV curve of MPK_2 possesses the largest integrate area, indicating its enlarged capacitive property. Electrochemical impedance spectroscopy (EIS) is performed to investigate the electron transport and ion diffusion [50]. Fig. S5b (Supporting information) shows the Nyquist plots of all MPK_x electrodes consisting of a little semicircle and vertical lines at the high- and low-frequency region separately. The equivalent series resistance (R_s) values derived from the Z'-intercept for MPK_x electrodes are almost identical of 1.11 Ω, while the charge-transfer resistance (R_{ct}) values inferred from the semicircle diameter are 1.16, 0.97, 0.48 and 0.82 Ω for MPK_0, MPK_1, MPK_2 and MPK_3, respectively. The lowest R_{ct} value of MPK_2 reflects rapid charge transfer arising from the conductive 3D framework in carbon nanosheets. The corresponding GCD profiles (Fig. S5c in Supporting information) for MPK_x electrodes at 1 A/g show nearly symmetrical isosceles triangles, further illustrating the existence of EDLC and pseudocapacitance, and MPK_2 displays the superior capacity calculated from the longest charge/discharge time. The CV curves with almost rectangular-shapes at various scan rates (Figs. S5d and S6a−c in Supporting information) and the corresponding GCD curves at various densities (Figs. S5e and S6d−f in Supporting information) of MPK_x demonstrate a satisfactory capacity and remarkable rate performance, implying the efficient electromigration of electrolyte ions to the electrode/electrolyte interphase. The specific capacitance of MPK_2 (Fig. S5f in Supporting information) at 10 A/g is 278 F/g (74.2% capacitance retention), indicating good rate performance. The excellent rate capability is attributed to rapid ions transport and short diffusion distance in open-developed porous carbon nanosheets, as well as a large ion-adsorption area and high-level heteroatom contents in carbon nanosheets skeleton.

To further assess the effect of N/O codoping on capacitive behaviors of MPK_2, the contributions of pseudocapacitance and EDLC are investigated. The total response current (i) with the scan rate (v) can be analyzed by the power-law relationship of $i = av^b$ [51,52]. The parameters of a and b are adjustable constants, and the b value ranging from 0.5 to 1 can be determined by the slope of log(i) *vs.* log(v) curves. When b-value is close to 0.5, it demonstrates the slow-kinetics behavior, whereas b-value of 1.0 represents a fast-kinetics process. The b-values are calculated to be 0.88 and 0.89 for charge and discharge process (Fig. S6a in Supporting information), indicating the co-existence of hybrid-kinetics behaviors. The pseudocapacitive- and EDLC-contributions for MPK_2 are further investigated and quantitatively analyzed according to the following equation $i(V) = k_1v + k_2v^{1/2}$ [53-55]. Where k_1v corresponds to the EDLC-controlled contribution and $k_2v^{1/2}$ represents the pseudocapacitance-dominant process. Figs. S7b and S8 (Supporting information) display the contributions of the EDLC-controlled in red region and the pseudocapacitive-dominant in green region at different scan rates. The MPK_2 electrode exhibits a 18.7% EDLC-controlled contribution ratio at a low scan rate of 10 mV/s and an increasing ratio of 42.1% at a relatively high scan rate of 100 mV/s (Fig. S7c in Supporting information), illuminating the superior ion storage capability of carbon nanosheets at high sweep rate. Therefore, the plentiful N/O heteroatoms codoping into the carbon nanosheets skeleton not only ameliorate the electrode/electrolyte interfacial compatibility, but also generate extra pseudocapacitance to increase the integral capability.

The MPK_2 electrode is further fabricate into the symmetric devices using 6 mol/L KOH and 1 mol/L H_2SO_4 as electrolyte to evaluate its practical application. The symmetrical behaviors in all the CV curves (Figs. S9a and c in Supporting information) and GCD profiles (Figs. S9b and d in Supporting information) during charge/discharge process are presented, indicating the excellent ion transmission efficiency and reversible capability. The relationship between capacitances and current densities is calculated from GCD profiles at 0.5–10 A/g and the profiles are shown in Fig. S9e (Supporting information). The symmetric device fabricated with H_2SO_4 electrolyte equips with a relatively high capacitance of 278 F/g at 0.5 A/g and a capacitance retention of 90% at 10 A/g, compared with the device assembled with KOH electrolyte (77% retention of initial capacitance). As shown in Fig. S9f (Supporting information), H_2SO_4 and KOH-loaded devices display low R_s value of 0.18 and 0.25 Ω, separately. Besides, the R_{ct} values of H_2SO_4 and KOH-loaded devices are 0.06 and 0.05 Ω, respectively. These results of MPK_2 electrode reveal the good conductivity, rapid electron transmission and high diffusion pathway for electrolyte ions. H_2SO_4-loaded device delivers a relatively larger energy output (11.4 Wh/kg, 250 W/kg) (Fig. S9h in Supporting information) than that of KOH-loaded device (8.9 Wh/kg) at the similar power density. The interface Faraday reactions of N/O species in acidic and/or basic electrolyte are shown in Fig. S9g (Supporting information). The long-term cyclic performance is satisfactory with the capacitance retention of 98.6% and 97.6% using KOH and H_2SO_4 after 5000 cycles at 1 A/g, respectively (Fig. S9i in Supporting information). Therefore, the superb electrochemical performance of carbon nanosheets can be ascribed to the unique 3D structures assembled with porous carbon nanosheets and the high-level heteroatoms decoration.

By comparison with acidic and/or basic electrolyte, N/O codoped carbon nanosheets generally exhibit a weak specific capacitance using water-in-salt electrolyte (15 mol/kg LiTFSI), owing to the absence of the Faraday redox reaction in a low OH^- and/or H^+ concentration [3,33]. Nevertheless, the lower concentration of H_2O molecules in LiTFSI which are strongly incorporated with Li^+, thereby facilitating the passivation of water decomposition [56,57]. The compatibility between multiscale porous N/O codoped carbon nanosheets and high concentrated LiTFSI electrolyte contributes to the symmetrical supercapacitor endowed with an enlarged stable voltage window and consequently a high-energy output. The maximum working voltage of MPK_2//MPK_2 device can reach to 2.25 V at 10 mV/s without obvious redox peaks derived from water decomposition (Fig. 4a), manifesting a high oxidative stability of water in LiTFSI electrolyte. The GCD profiles at 0.5–10 A/g (Fig. 4b and Figs. S10e−g in Supporting information) and the CV curves at 10–100 mV/s (Figs. S10a−d in Supporting information) reveal the excellent rate capacity and high reversibility of MPK_x electrodes. The ionic conductivity and viscosity of the 15 m LiTFSI electrolyte are 10.8 mS/cm and 0.022 Pa·s respectively, which reveals the passivate ion migration within the hierarchical porous channels [58]. When the current density is progressively increased from 0.5 A/g to 8 A/g, H_2SO_4-based device (Fig. S11 in Supporting information) possesses a high-quality capacitance of 320 F/g with a capacitance retention of 86.8% compared with KOH- (79.3%) and LiTFSI-based devices (56.2%), revealing that the low viscosity and high conductivity benefit to a rapid ion kinetics within hierarchical porous nanosheets architecture and thereby result in the excellent rate capability. The interfacial contact resistance for MPK_2 electrode in Fig. 4c is ∼1.2 Ω, revealing efficient electron transfer. In addition, the relaxation time constant (τ) is 16 s (Fig. 4d), indicating a well-defined response of MPK_2-based supercapacitor. The durability (Fig. 4e) is characterized and the capacitance of MPK_2 electrode still retains

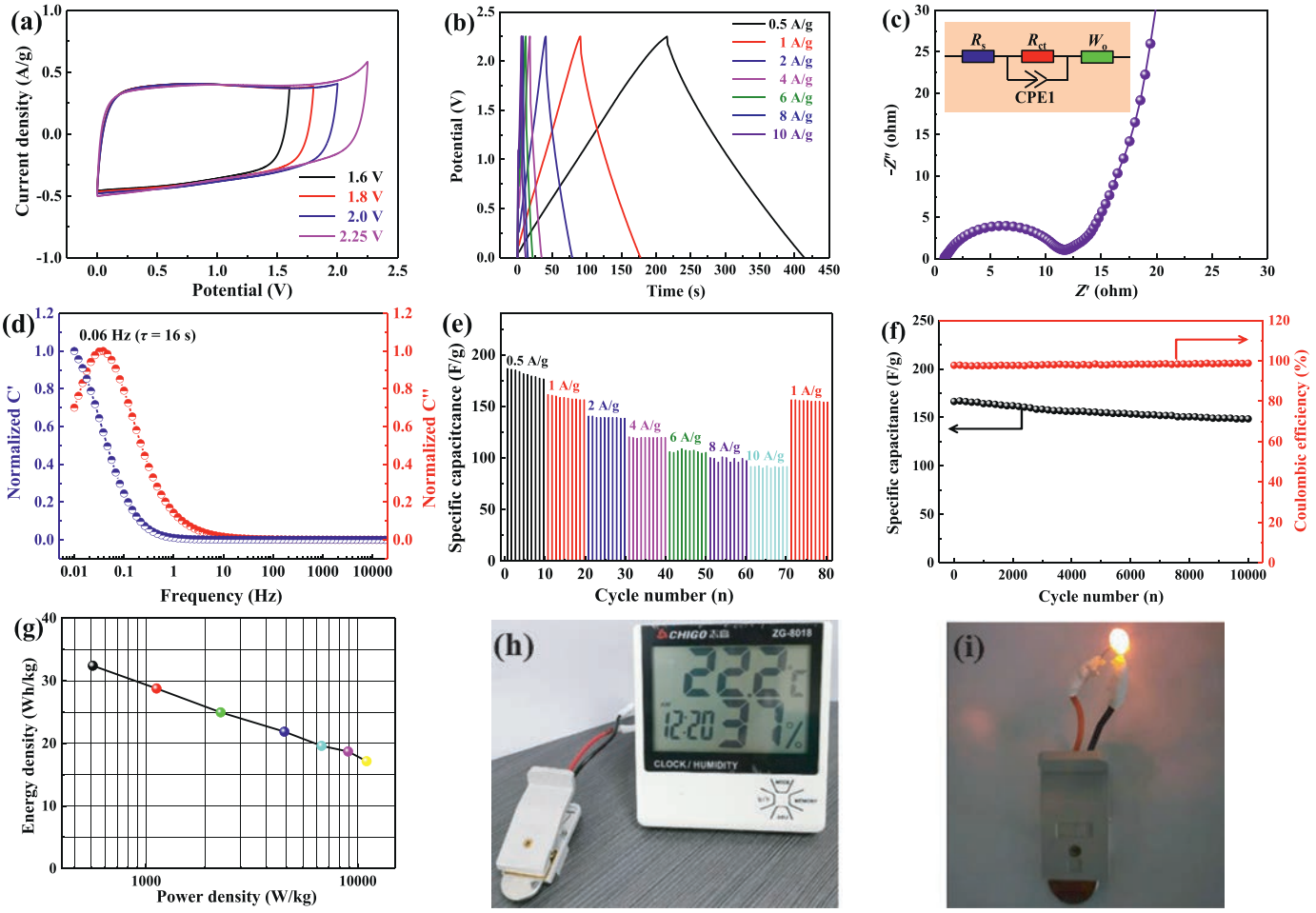

Fig. 4. The electrochemical performances of MPK_2-based device: CV curves at different voltage windows at 10 mV/s (a), GCD curves (b), Nyquist plots (c), the normalized real and imaginary part capacitance (d), cyclic stability at different current densities (e), cycling performance at 1 A/g (f), Ragone plots (g) and photograph of thermohygrograph and LED powered by the MPK_2//MPK_2 supercapacitors (h, i).

165 F/g at 1 A/g with ~97% retention of initial value after consecutive 70 cycles, indicating the exceptional durability. The long-term cyclicality and high coulombic efficiency are displayed in Fig. 4f. Even after 10000 cycles, the capacitance retention preserves 91% and coulombic efficiency is about 98%, demonstrating the satisfactory cycling performance. The MPK_2-based device harvests an enlarged energy delivery of 33.1 Wh/kg (550 W/kg) (Fig. 4g), outperforming other sheet-like carbon-loaded supercapacitors (Table S3 in Supporting information). Furthermore, the thermohygrograph can be successfully driven to detect the temperature and humidity in the room by the fully charged MPK_2//MPK_2 device using LiTFSI electrolyte (Fig. 4h). Meanwhile, the 2.0 V red light-emitting diode (LED) can be easily lighted by MPK_2//MPK_2 device (Fig. 4i), indicating the potential application for efficient energy storage devices.

Overall, the MPK_2 electrode exhibits the high specific capacitance, supreme rate capacity and excellent cyclicality, which ascribed to its architectural advantages. First, the interconnected carbon nanosheets contribute to the enhancement of the electroconductivity of the electrode, resulting in satisfactory rate capability and excellent cyclic performance [59,60]. Second, the enlarged ion-adsorption surface area and the compatibility between porous surface of N/O codoped carbon nanosheets and high concentrated LiTFSI electrolyte facilitate the fast ion permeation and sorption, thereby conducing to efficient charge accumulation [61,62]. Third, the abundant N/O dopants not only enhance the ion-accessibility of electrode/electrolyte interphase by lavish electron density, but also generate extra pseudocapacitance through Faraday redox reaction for the enhancement of integral capacitance [63,64].

In conclusion, hierarchical porous carbon nanosheets with N/O codoping derived from copolycondensation of aldehyde-amine-quinone are successfully fabricated through varying the feed ratio of comonomers. The robust carbon nanosheets framework generating from π-conjugated aromatic rings and conjugated-bond in copolymers are preserved during annealing, resulting in the enlarged ion-adsorption surface area (1630 m^2/g), open-ended porous architecture and enriched N/O codoping contents (N: 3.58 at%, O: 12.91 at%). Integrating the advantageously structural features with electroactive heteroatoms species in the typical MPK_2 electrode furnishes the assembled symmetric device with a high energy generation of 11.4 Wh/kg in H_2SO_4 electrolyte. Furthermore, the compatibility between typical carbon nanosheets and concentrated LiTFSI leads to the 2.25 V MPK_2-loaded device exhibiting an enhanced energy delivery (33.1 Wh/kg), demonstrating that N/O codoped porous carbon nanosheets assembled supercapacitor has a great potential for the practical electrical devices.

Declaration of competing interest

The authors declare that they have no known competing financial interests or personal relationships that could have appeared to influence the work reported in this paper.

Acknowledgments

This work is financially supported by the National Natural Science Foundation of China (Nos. 21875165, 51772216, 22172111 and 21905207), the Science and Technology Commission of Shanghai Municipality, China (Nos. 20ZR1460300, 14DZ2261100), Anhui University of Science and Technology Introduced Talent Research Startup Fund (No. 13210572), Zhejiang Provincial Natural Science Foundation of China (No. LY19B010003), the Fundamental Research Funds for the Central Universities and the Large Equipment Test Foundation of Tongji University.

Supplementary materials

Supplementary material associated with this article can be found, in the online version, at doi:10.1016/j.cclet.2021.08.123.

References

[1] X. Yang, J. Mao, H. Niu, et al., Chem. Eng. J. 406 (2021) 126713.
[2] H. Zhang, X. He, F. Wei, et al., ACS Sustainable Chem. Eng. 8 (2020) 3065–3071.
[3] L. Ji, B. Wang, Y. Yu, et al., Electrochim. Acta 331 (2020) 135348.
[4] X. Dong, H. Jin, R. Wang, et al., Adv. Energy Mater. 8 (2018) 1702695.
[5] J. Zhao, H. Lai, Z. Lyu, et al., Adv. Mater. 27 (2015) 3541–3545.
[6] Z. Song, L. Miao, L. Ruhlmann, et al., Adv. Mater. 33 (2021) 2104148.
[7] J. Bai, B. Xi, H. Mao, et al., Adv. Mater. 30 (2018) 1802310.
[8] Z. Song, L. Miao, L. Li, et al., Carbon 180 (2021) 135–145.
[9] C. Li, W. Wu, P. Wang, et al., Adv. Sci. 6 (2019) 1801665.
[10] K.A. Owusu, Z. Wang, L. Qu, et al., Chin. Chem. Lett. 31 (2020) 1620–1624.
[11] F. Wang, L. Chen, H. Li, et al., Chin. Chem. Lett. 31 (2020) 1986–1990.
[12] J. Zhu, K. Sakaushi, G. Clavel, et al., J. Am. Chem. Soc. 137 (2015) 5480–5485.
[13] Z. Bo, W. Zhu, W. Ma, et al., Adv. Mater. 25 (2013) 5799–5806.
[14] Y. Liu, H. Zhang, H. Song, et al., J. Phys. Chem. C 121 (2017) 23947–23954.
[15] M. Liu, J. Niu, Z. Zhang, et al., Nano Energy 51 (2018) 366–372.
[16] F. Wei, X. He, H. Bi, et al., J. Power Sources 474 (2020) 228698.
[17] L. Chen, Y. Liu, Z. Deng, et al., Sci. China Mater. 64 (2021) 96–104.
[18] X. Xi, D. Wu, L. Han, et al., ACS Nano 12 (2018) 5436–5444.
[19] B. Li, B. Xi, F. Wu, et al., Adv. Energy Mater. 9 (2019) 1803070.
[20] H. Peng, B. Yao, X. Wei, et al., Adv. Energy Mater. 9 (2019) 1803665.
[21] X. Zheng, J. Luo, W. Lv, et al., Adv. Mater. 27 (2015) 5388–5395.
[22] S. Feng, J. Song, C. Zhu, et al., ACS Appl. Mater. Interfaces 11 (2019) 5911–5918.
[23] R. Hou, B. Liu, Y. Sun, et al., Nano Energy 72 (2020) 104728.
[24] S. Sun, F. Han, X. Wu, et al., Chin. Chem. Lett. 31 (2020) 2235–2238.
[25] L. Miao, H. Duan, D. Zhu, et al., J. Mater. Chem. A 9 (2021) 2714–2724.
[26] C. Huang, A. Hu, Y. Li, et al., Nanoscale 11 (2019) 16515–16522.
[27] Y. He, X. Zhuang, C. Lei, et al., Nano Today 24 (2019) 103–119.
[28] G. Yuan, Y. Liang, H. Hu, et al., ACS Appl. Mater. Interfaces 11 (2019) 26946–26955.
[29] Y. Chen, I. Kone, Y. Gong, et al., Carbon 152 (2019) 325–334.
[30] T. Liang, R. Hou, Q. Dou, et al., Adv. Funct. Mater. 30 (2020) 2006749.
[31] J. Park, Y.E. Yoo, L. Mai, et al., ACS Sustainable Chem. Eng. 7 (2019) 7728–7735.
[32] X. Bu, L. Su, Q. Dou, et al., J. Mater. Chem. A 7 (2019) 7541–7547.
[33] L. Suo, O. Borodin, T. Gao, et al., Science 350 (2015) 938–943.
[34] Y. Shen, B. Liu, X. Liu, et al., Energy Storage Mater. 34 (2021) 461–474.
[35] R. Zhang, X. Jing, Y. Chu, et al., J. Mater. Chem. A 6 (2018) 17730–17739.
[36] J. Yan, L. Miao, H. Duan, et al., Electrochim. Acta 358 (2020) 136899.
[37] Y. Shu, J. Maruyama, S. Iwasaki, et al., J. Power Sources 364 (2017) 374–382.
[38] H. Lin, W. Ye, Y. Liu, et al., J. Mater. Chem. A 8 (2020) 1221–1228.
[39] T. Zhu, D. Liu, L. Shi, et al., ACS Appl. Mater. Interfaces 12 (2020) 34910–34918.
[40] Z. Liu, H. Song, Y. Zhao, et al., ACS Mater. Lett. 1 (2019) 290–296.
[41] L. Chen, C. Lian, H. Jiang, et al., Chem. Eng. Sci. 217 (2020) 115496.
[42] Y. Liu, Z. Xiao, Y. Liu, et al., J. Mater. Chem. A 6 (2018) 160–166.
[43] G. Ping, L. Miao, A. Awati, et al., Chin. Chem. Lett. 32 (2021) 3811–3816.
[44] F. Hu, T. Zhang, J. Wang, et al., Nano Energy 74 (2020) 104789.
[45] C. Long, L. Miao, D. Zhu, et al., ACS Appl. Energy Mater. 4 (2021) 5727–5737.
[46] Z. Xu, Y. Liu, H. Chen, et al., J. Mater. Sci. 52 (2017) 7781–7793.
[47] L. Yao, Q. Wu, P. Zhang, et al., Adv. Mater. 30 (2018) 1706054.
[48] H. Mao, L. Liu, L. Shi, et al., Sci. Bull. 65 (2020) 803–811.
[49] Q. Li, R. Jiang, Y. Dou, et al., Carbon 49 (2011) 1248–1257.
[50] X. Wei, J.S. Wei, Y. Li, et al., J. Power Sources 414 (2019) 13–23.
[51] J. Chen, B. Yang, H. Hou, et al., Adv. Energy Mater. 9 (2019) 1803894.
[52] H. Niu, Q. Yang, Q. Wang, et al., Nano Energy 78 (2020) 105360.
[53] B. Sun, S. Lou, Z. Qian, et al., Nano Energy 66 (2019) 104179.
[54] Y. Chang, H. Shi, X. Yan, et al., Carbon 170 (2020) 127–136.
[55] Z. Li, D. Chen, Y. An, et al., Energy Storage Mater. 28 (2020) 307–314.
[56] K. Mahankali, N.K. Thangavel, Y. Ding, et al., Electrochim. Acta 326 (2019) 134989.
[57] S.W. Xu, M.C. Zhang, G.Q. Zhang, et al., J. Power Sources 441 (2019) 227220.
[58] J. Tan, M. He, G. Zhang, IEEE Power Energ. Soc. Gen. Meet. (PESGM) (2020) 1–5.
[59] J. Liu, J. Wang, C. Xu, et al., Adv. Sci. 5 (2018) 1700322.
[60] Y. Li, S. Liu, Y. Liang, et al., ACS Sustainable Chem. Eng. 7 (2019) 13827–13835.
[61] J. Hou, K. Jiang, R. Wei, et al., ACS Appl. Mater. Interfaces 9 (2017) 30626–30634.
[62] Y. Lin, Z. Chen, C. Yu, et al., ACS Sustainable Chem. Eng. 7 (2019) 3389–3403.
[63] D. Hulicova-Jurcakova, M. Seredych, G.Q. Lu, et al., Adv. Funct. Mater. 19 (2009) 438–447.
[64] Y.P. Zhao, R.X. Xu, J.P. Cao, et al., J. Electroanal. Chem. 871 (2020) 114288.